

# PALTO: Physics-Informed Active Learning for Tri-Gate FinFET Design Optimization for Vertical Power Delivery

Ayoub Sadeghi 

University of Illinois Chicago  
Chicago, USA  
asadeg3@uic.edu

Leonid Popryho 

University of Illinois Chicago  
Chicago, USA  
lpopry2@uic.edu

Inna Partin-Vaisband 

University of Illinois Chicago  
Chicago, USA  
vaisband@uic.edu

**Abstract**—This paper demonstrates the effectiveness of machine learning-driven optimization for designing application-specific GaN tri-gate FinFETs in vertical power delivery systems. Conventional TCAD-based approaches are computationally intensive and insufficient for navigating the high-dimensional, nonlinear design space of advanced GaN devices. To address this, a physics-informed active learning framework is used to intelligently guide simulations, accelerating convergence while preserving accuracy. This ML-guided approach enables the discovery of optimal configurations by efficiently exploring key structural parameters—most notably the GaN-to-AlGaN thickness ratio—a long-standing focus of debate in device design. By systematically exploring key structural parameters, two optimized devices with aggressively scaled gate-to-drain lengths are identified. Single-fin, multi-channel simulations show that device D2, with a thinner GaN channel relative to the AlGaN barrier, achieves higher drive current. However, in a 300-fin configuration, device D1 outperforms device D2 by delivering 3.3A at 0.49 ohm on-resistance—approximately  $2\times$  better—despite slightly higher parasitics. Both devices operate in a normally-off mode. Based on an application-specific figure of merit, device D1 achieves 5pC-ohm, demonstrating  $2\times$  greater switching efficiency than device D2, while both designs outperform industrial benchmarks from different performance standpoints.

**Keywords**—power transistors, junction capacitances, e-mode operation, tri-gate FinFET GaN, multi-channel.

## I. INTRODUCTION

The growing demand for efficient power delivery in next-generation computing platforms has driven the adoption of vertical power delivery (VPD) architectures, where power switches are strategically integrated directly beneath the functional die to minimize interconnect losses and improve power density (see Fig. 1(a)) [1], [2]. To effectively enable VPD approaches, compact, high-performance power switches should be embedded in close proximity to points-of-load (POLs),

thereby reducing energy losses and enhancing system efficiency [3]–[8].

Among the various device candidates, multi-fin, multi-channel tri-gate GaN FinFETs have emerged as a highly promising solution due to their superior scalability and ability to sustain high current densities [3], [9]–[15]. Their performance builds upon the capabilities demonstrated by single-fin, multi-channel GaN FinFET units, which serve as the foundational elements of the design (see Fig. 1(b)(c)) [3], [9].

Albeit the initial promise, GaN switches that meet the stringent VPD performance requirements in modern systems-on-package (SoPs) and chiplet-based systems have not yet demonstrated. Particularly, performance targets include large voltage conversion ratios (e.g., stepping down from 48 V or 12 V to 1 V), current densities exceeding  $2\text{--}4\text{ A/mm}^2$ , enhancement mode (E-mode) operation, and conversion efficiencies in the range of 90%–93%. To achieve the required efficiency, switching and conduction losses should be carefully balanced, posing additional design constraints on parasitic resistance and capacitances in such devices [16].

Optimization of complex multi-fin multi-channel devices relies on precise co-design of key structural single-channel device parameters, requiring numerous iterations of extensive simulations [3], [10], [14], [17] (see Fig. 1(b)). Traditional TCAD-based exploration is, however, computationally expensive and poorly suited for navigating the highly nonlinear, high-dimensional design space [3], [10]. These limitations often result in suboptimal solutions, especially for non-planar GaN devices in VPD systems. Instead, intelligent, data-efficient optimization strategies and design space exploration techniques are required to efficiently navigate complex, high-dimensional parameter landscapes and identify optimal device configurations.

To address this challenge, a physics-informed machine learning (ML) framework is proposed in this paper. The workflow of the framework is illustrated in Fig. 2. The framework was developed and trained on a systematically generated TCAD dataset. The model effectively captures complex,

This work was supported by the Center for Heterogeneous Integration of Micro Electronic Systems (CHIMES), one of seven centers in Joint University Microelectronics Program (JUMP) 2.0, a Semiconductor Research Corporation (SRC) program sponsored by the Defense Advance Research Project Agency (DARPA). We thank Prof. Debjit Pal for providing the distributed simulation infrastructure.

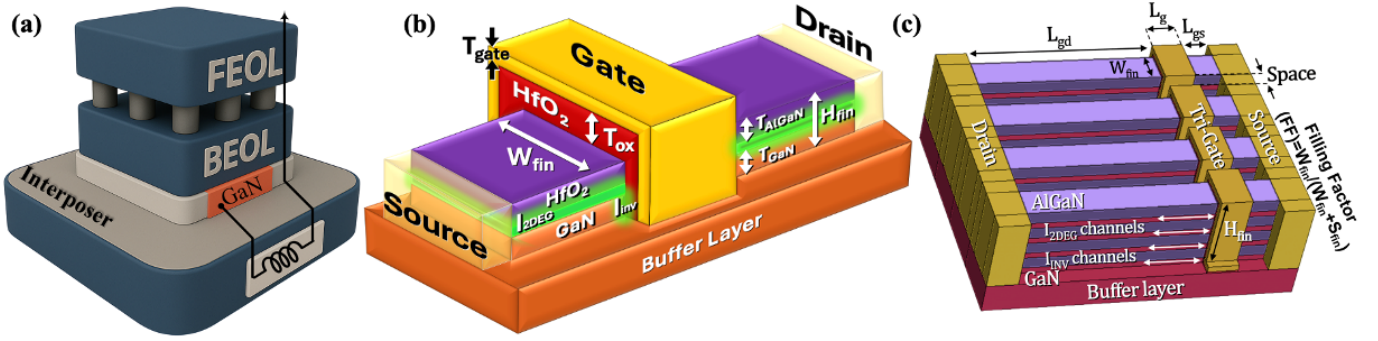


Fig. 1. Vertical power delivery, (a) system architecture with GaN power switches integrated beneath the functional die [3], (b) tri-gate FinFET with a single fin and single channel, illustrating key design parameters, and (c) multi-fin configuration of the tri-gate FinFET with four parallel channels.

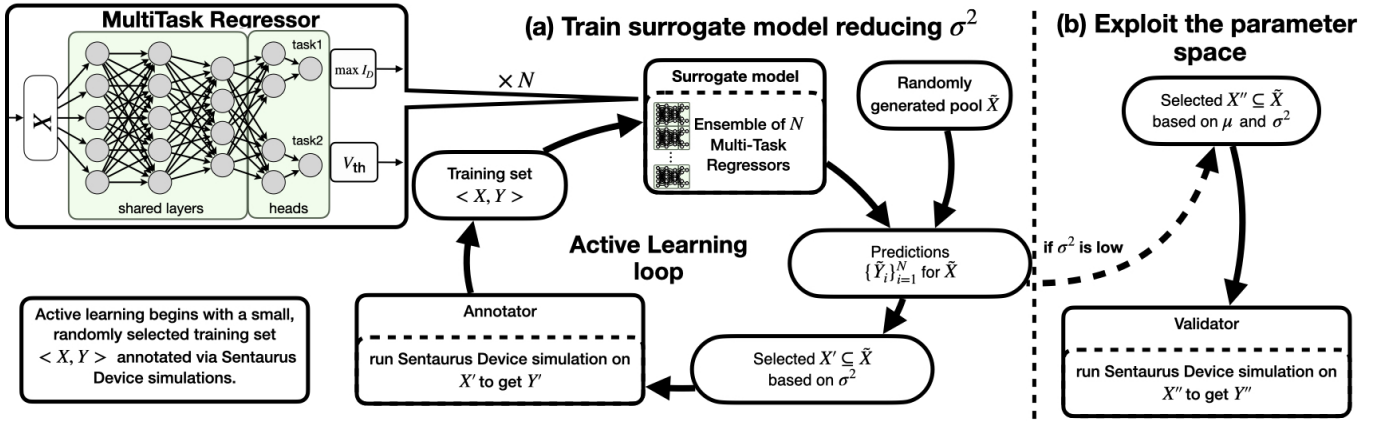


Fig. 2. PALTO active-learning workflow, (a) exploration (i.e., candidate selection and labeling using an ensemble of multi-task regressors), and (b) exploitation (i.e., selection of high-performance, low-uncertainty designs using the trained model).

nonlinear dependencies between structural device parameters and performance metrics, enabling rapid, targeted exploration of the design space. Compared to conventional methods, the ML-guided approach significantly reduces simulation time and computational overhead, while providing valuable physical insights into how critical features—such as layer thicknesses, channel geometry, and doping profiles—impact switching efficiency [18]. Additional insight is gained by calculating SHAP (SHapley Additive exPlanations) values, a game theory-based method that quantifies how much each input feature (e.g., a device parameter or design variable) contributes to the model’s output or decision (see Fig. 3).

By targeting high output current ( $I_{DS}$ ) and a positive threshold voltage ( $V_{th}$ ), the ML-guided optimization process identifies two distinct device configurations, named as device D1 and device D2, primarily differentiated by the thicknesses of the GaN channel and AlGaIn barrier—a primary challenge among similar device optimizations [19]. Device D1 features a structure with thicker GaN, while device D2 employs a thicker AlGaIn barrier relative to the GaN channel. When scaled to a 300-fin architecture (see Fig. 1(c)), device D1 achieves  $R_{on} = 0.49 \Omega$  and  $I_{DS} = 3.3 \text{ A}$ , compared to  $0.94 \Omega$  and  $1.67 \text{ A}$  for device D2—both outperforming the non-ML-optimized baseline [3] and commercial benchmarks. Addition-

ally, both designs exhibit low parasitic capacitances, offering a scalable and high-performance solution for integration of GaN power transistors into next-generation compute platforms.

## II. PALTO METHODOLOGY

While TCAD simulations offer accurate device-level physics, a TCAD-based evaluation of a set of device parameters requires on average 16 minutes and up to 6.25 hours for those more complex nonlinear settings (see Fig. 4). Brute-force exploration of such design space is, therefore, impractical. To overcome this, the **PALTO** (Physics-Informed Active Learning for Tri-Gate FinFET Optimization) framework is introduced. It couples a query-by-committee active learning loop with a deep-ensemble surrogate model, prioritizing high-value candidates for TCAD evaluation while screening millions of low-uncertainty variants in seconds.

Each simulation is an expensive to evaluate function  $f_{TCAD} : \mathbf{x} \mapsto \{I_{DSmax}, V_{th}\}$ , where  $\mathbf{x}$  covers the ranges in Table I. An initial Latin Hypercube Sampling (LHS) [20]—a statistical method for generating representative samples from a multi-dimensional parameter space—of about  $10^3$  different device configurations (guided by [3], [18]) with corresponding simulated  $I_{d,max}$  and  $V_{th}$  results is used to bootstrap the surrogate model.

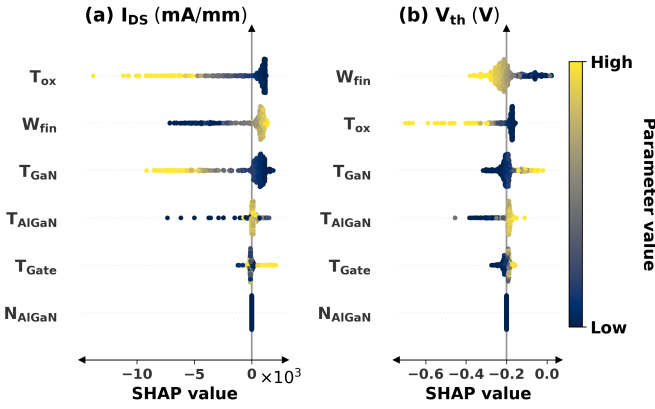


Fig. 3. SHAP beeswarm plots for (a)  $I_{DS,max}$  and (b)  $V_{th}$ , where positive (negative) values indicate increasing (decreasing) contribution of device parameters. The plots reveal that  $T_{ox}$  and  $W_{fin}$  dominate both metrics, with opposing trends between them.

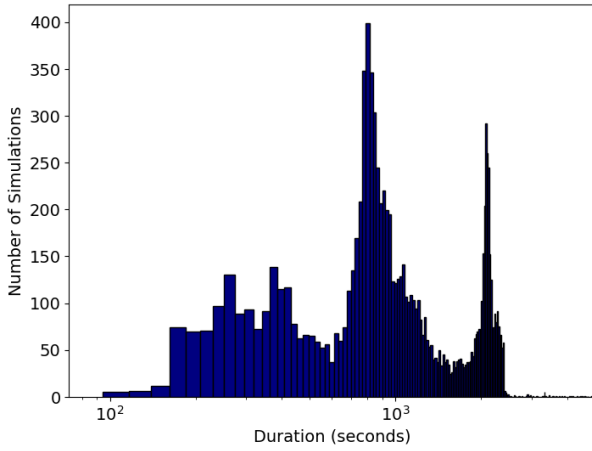


Fig. 4. Distribution of TCAD simulation runtimes across all completed trials. Individual runs span from 1.5 min to 6 h 15 min, with a heavy-tailed spread and a median of  $\sim 16$  min.

A multitask neural network with a shared fully-connected backbone and two task-specific heads simultaneously predicts  $I_{DS,max}$  and  $V_{th}$ . To balance the multi-objective loss function, training uses homoscedastic-uncertainty weighting, a technique that balances multiple loss terms by modeling each task’s constant output uncertainty [21].

$$\mathcal{L} = \frac{\|I_{DS,max} - \hat{I}_{DS,max}\|^2}{2\sigma_I^2} + \frac{\|V_{th} - \hat{V}_{th}\|_w^2}{2\sigma_V^2} + \log \sigma_I + \log \sigma_V \quad (1)$$

with an additional ten-fold penalty applied to errors where  $V_{th} > 0$  in order to maintain high accuracy in the enhancement-mode regime. An ensemble of  $N = 10$  such networks captures epistemic uncertainty, which reflects the model’s lack of knowledge due to limited training data, finite model capacity, and imperfect underlying assumptions,

$$\mathcal{U}(\mathbf{x}) = \text{Var}\{M_i(\mathbf{x})\}_{i=1}^N. \quad (2)$$

After convergence ( $R^2 > 0.98$  on both tasks), the ensemble is able to predict  $6 \times 10^9$  designs in about 10 minutes on a single RTX 4090, while only around  $10^4$  TCAD calls are required for convergence in total. All runs, metrics, and artifacts are tracked with Weights & Biases (W&B)—a platform for experiment tracking, hyperparameter tuning, and reproducibility—to ensure that the modeling workflow is reproducible, well-logged, and version-controlled, thus improving transparency and auditability of results.

The algorithm adopts a query-by-committee strategy (see Algorithm 1), where deep-ensemble is used to estimate epistemic uncertainty and guide the selection of informative samples [22], [23].

---

#### Algorithm 1 PALTO active-learning loop

---

- 1: The labeled pool  $\mathcal{D}_0$  is initialized with  $k$  uniformly distributed simulations
  - 2: **for** round  $t = 1$  until validation uncertainty stabilizes **do**
  - 3: The deep-ensemble surrogate  $\{M_i\}_{i=1}^N$  is trained on  $\mathcal{D}_{t-1}$
  - 4: A large candidate pool of size  $n$  is drawn over the design space and the uncertainty score  $\mathcal{U}(\mathbf{x})$  is evaluated
  - 5: Candidates are ranked by  $\mathcal{U}$ ; a greedy farthest-first filter selects a diverse subset of  $m$  points
  - 6: High-fidelity TCAD simulations are executed for these  $m$  and the results are appended to form  $\mathcal{D}_t$
  - 7: **end for**
- 

**Experimental setup.** In the reported study, the initial pool comprised approximately  $k = 10^3$  uniformly sampled devices; each iteration assessed  $n = 10^6$  randomly drawn candidates, from which batches of  $m = 100$  designs were simulated with Sentaurus before retraining. The loop terminated once the ensemble variance on a held-out validation grid stops decreasing.

Prediction variance alone tends to cluster similar candidates. Before each TCAD batch, a greedy farthest-first pass is applied to maximize the minimum pair-wise  $L_2$  distance in the parameter space, pruning redundant candidates without information loss.

SHAP beeswarm plots (Fig. 3) computed on the converged ensemble with `shap.DeepExplainer` are utilized to rank the dominant features for (a)  $I_{DS,max}$  and (b)  $V_{th}$ . Each point represents an deck (i.e., a set of input parameters); color encodes the raw feature value, and the x-axis shows the signed contribution relative to a reference.

Compared with NSGA-II [24], a widely used multi-objective evolutionary algorithm for identifying Pareto-optimal solutions under conflicting objectives, used here to maximize  $I_{DS}$  under the constraint  $V_{th} > 0$ , and random search, PALTO achieves a  $3.2\times$  reduction in TCAD cost to reach equivalent

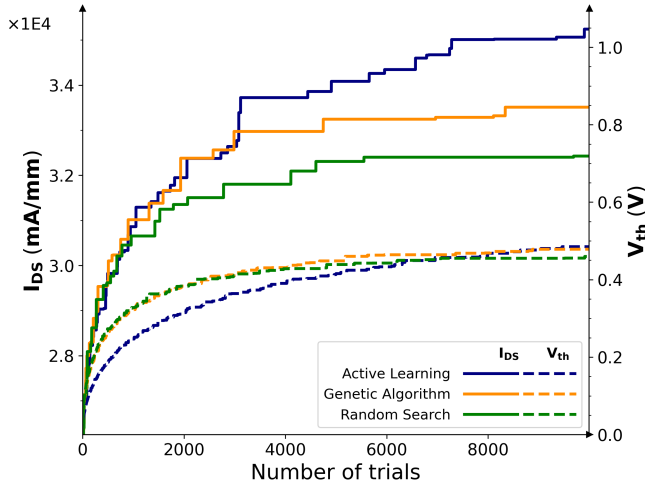


Fig. 5. Convergence of best  $I_{DSmax}$  (solid) and  $V_{th}$  (dashed) versus cumulative TCAD calls; PALTO compared with NSGA-II and random search.

or superior device performance (see Fig. 5). Based on the learned design landscape (Fig. 6), two devices meeting the design targets are identified for comprehensive DC and AC evaluation, in 50-device multi-fin parallel configuration.

### III. DEVICE STRUCTURE AND RESULTS

A state-of-the-art baseline configuration [3] and the two identified optimal devices (see Table I for a list of key design parameters) share a gate length ( $L_g$ ) of  $0.1 \mu\text{m}$  and a gate-to-drain spacing ( $L_{gd}$ ) of  $0.6 \mu\text{m}$ , resulting in a total device length of approximately  $1 \mu\text{m}$ . Reducing  $L_{gd}$  enhances the drive current and lowers the on-resistance ( $R_{on}$ ), albeit at the cost of reduced breakdown voltage (BV). However, for the targeted power delivery application, a BV of above  $50 \text{ V}$  remains acceptable. All devices employ  $\text{HfO}_2$  as the gate dielectric and utilize an AlGaIn barrier layer with a composition of  $\text{Al}_{0.25}\text{Ga}_{0.75}\text{N}$ . Device parameters are normalized to the effective width ( $W_{eff} = 2H_{fin} + W_{fin}$ ) for consistent performance comparison. The optimization intervals and the final parameter values of the individual devices are listed in Table I, highlighting the structural differences between the two optimized configurations. All simulations are performed using 3D TCAD Sentaurus. To ensure accurate representation of electrostatics and carrier transport, advanced physical models, such as Shockley-Read-Hall (SRH) recombination, interface trap modeling, and finite element methods (FEM) dynamics are incorporated [3], [10].

**Single-Fin Configuration.** Temperature-dependent transfer characteristics ( $I_{DS}-V_{GS}$ ) of the two optimized single-fin four-channel devices are shown in Fig. 7 for variety of  $V_{DS}$  values. As temperature increases,  $I_{DS}$  decreases and  $V_{th}$  shifts negatively, as further illustrated in Fig. 7. Despite this negative shift, both devices maintain E-mode operation, demonstrating strong thermal stability.

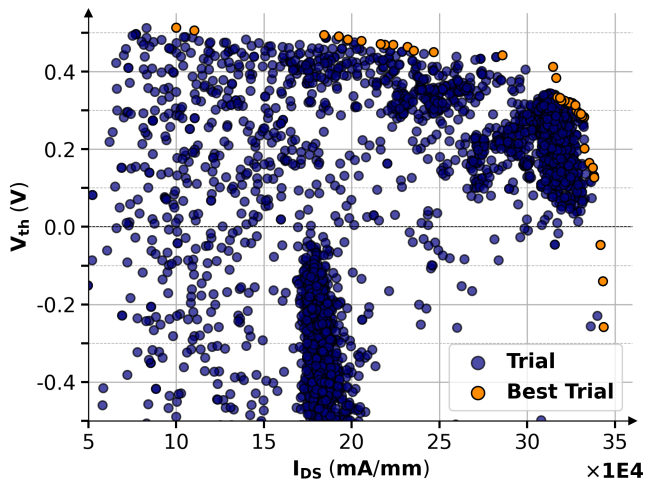


Fig. 6. Simulated performance for all explored tri-gates. Pareto front clusters along the upper-right boundary, indicating simultaneous improvement  $I_{DSmax}$  and  $V_{th}$  metrics within the explored design space.

TABLE I  
KEY DESIGN PARAMETERS AND THEIR RESPECTIVE INTERVALS USED IN THE EXHAUSTIVE SIMULATION PROCEDURE, COMPARED AGAINST THOSE SELECTED BY THE ML-BASED METHOD FOR OPTIMAL DEVICE IDENTIFICATION.

Description	Extensive Simulation Baseline [3]	ML-Based		
		Optimization Interval	Selected Devices	
			D1	D2
Doping ( $10^{18}\text{cm}^{-3}$ )	1	1 ... 100	17.1	94
Fin width (nm)	100	10 ... 250	87	81
GaN thickness (nm)	20	10 ... 100	99	11
AlGaIn thickness (nm)	40	10 ... 100	83	95
Oxide thickness (nm)	6	5 ... 25	6	5
Gate thickness (nm)	20	5 ... 40	5	37
Number of channels	4	4	4	4

Specifically, device D1 exhibits a peak current of  $14,101 \text{ mA/mm}$  at  $25^\circ\text{C}$  and  $V_{DS} = 12 \text{ V}$ , which is approximately  $14\%$  higher than its performance at  $V_{DS} = 5 \text{ V}$ . It also shows fast current saturation and minimal degradation with increasing temperature. Device D2 achieves a significantly higher peak current of  $76,105 \text{ mA/mm}$  at  $25^\circ\text{C}$  and  $V_{DS} = 12 \text{ V}$ , featuring a wider  $V_{GS}$  range that makes it well-suited for linear-region operation—a preferred mode for power switching—while maintaining similarly low temperature-induced degradation. Device D1 exhibits a total  $V_{th}$  shift of  $0.25 \text{ V}$  from  $25^\circ\text{C}$  to  $150^\circ\text{C}$  at  $V_{DS} = 5 \text{ V}$  and  $12 \text{ V}$ , indicating good thermal stability. In contrast, device D2 shows a slightly larger shift of  $0.57 \text{ V}$  at  $V_{DS} = 5 \text{ V}$  and  $0.43 \text{ V}$  at  $V_{DS} = 12 \text{ V}$ , attributed to its higher gate-to-oxide thickness ratio. Yet  $V_{th}$  remains positive across temperature and bias voltages, confirming the normally-off behavior of both devices. Overall, device D2 delivers a higher  $I_{DS}$  and maintains a more stable  $V_{th}$  across a wider  $V_{GS}$  range, making it more suitable for high-temperature applications.

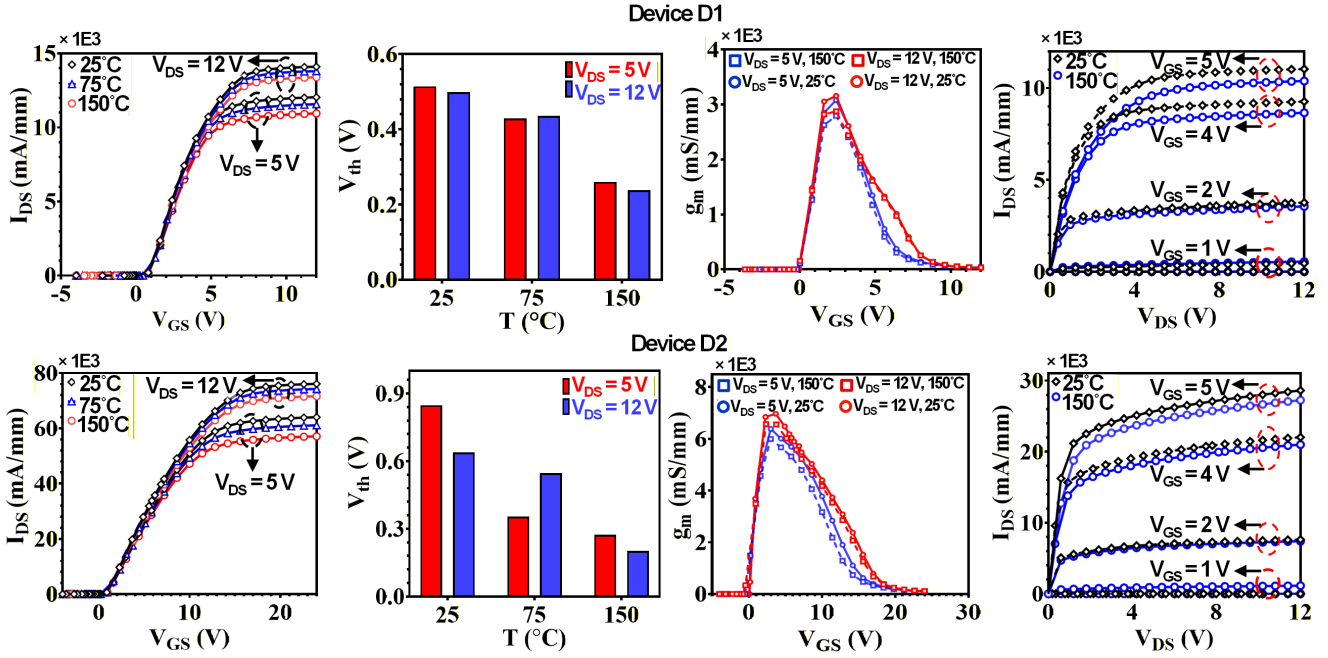


Fig. 7. Temperature-dependent performance of the optimized single-fin, multi-channel devices D1 and D2 with  $L_{gd} = 0.6 \mu\text{m}$  and  $L_g = 0.1 \mu\text{m}$ . The results demonstrate stable operation across the voltage and temperature ranges of interest.

To evaluate the high-frequency suitability of scaled-down  $L_{gd}$  tri-gate devices, Fig. 7 presents the extracted at  $V_{DS} = 5 \text{ V}$  and  $12 \text{ V}$  transconductance ( $g_m$ ). Device D2 exhibits a higher peak  $g_m$ , reaching up to  $7,000 \text{ mS/mm}$  at  $25^\circ\text{C}$  and maintaining  $6,500 \text{ mS/mm}$  at  $150^\circ\text{C}$ . This indicates strong gate control and suitability for high-frequency operation. Device D1 demonstrates a peak  $g_m$  of approximately  $3,000 \text{ mS/mm}$  with minimal temperature degradation, showing stable transconductance across the operating range. These results confirm that device D2 offers enhanced performance, comparable to similarly sized reported devices [3], [10], [14].

The  $I_{DS}$ - $V_{DS}$  output characteristics of device D1 and device D2 are shown for  $L_{gd} = 0.6 \mu\text{m}$  in Fig. 7 as a function of  $V_{GS}$  and temperature. Device D1 reaches a maximum  $I_{DS}$  of  $11,039 \text{ mA/mm}$  at  $V_{DS} = 12 \text{ V}$  and  $V_{GS} = 5 \text{ V}$ , while device D2 achieves a significantly higher peak of  $28,609 \text{ mA/mm}$ . Thus, device D2 consistently delivers higher  $I_{DS}$  across all gate biases and temperature conditions, demonstrating superior current drive and improved thermal robustness. Both devices exhibit early current saturation and reduced temperature sensitivity at higher gate overdrives.

The impact of aggressive gate length ( $L_g$ ) scaling and gate-to-drain ( $L_{gd}$ ) spacing is shown in Fig. 8, yielding a consistent increase in  $I_{DS}$  with decreasing device dimensions across temperature conditions and  $V_{DS}$  values. Notably, at  $V_{DS} = 12 \text{ V}$ , device D2, with  $L_g = 0.1 \mu\text{m}$  and  $L_{gd} = 0.6 \mu\text{m}$ , achieves peak  $I_{DS}$  of  $28,609 \text{ mA/mm}$ , compared to  $24,565 \text{ mA/mm}$  at  $L_g = 0.1 \mu\text{m}$  and  $L_{gd} = 4 \mu\text{m}$ , maintaining strong performance even at elevated temperatures. The high current drive capability

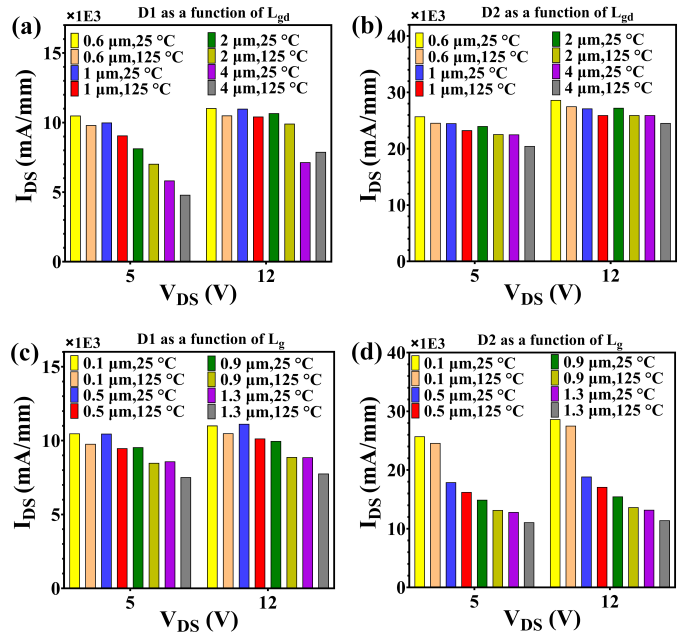


Fig. 8. impact of  $L_{gd}$  and  $L_g$  on maximum current for devices D1 and D2, showing that larger  $L_{gd}$  and  $L_g$  reduce  $I_{DS}$ , more significantly in D2 and at  $125^\circ\text{C}$ .

combined with manageable thermal degradation highlights the potential of such aggressively scaled designs for high-performance power applications.

Electrical and small-signal analyses comparing the proposed and baseline [3], [11] devices are summarized in Table II. The DC performance comparison highlights significant improve-

ments in the optimized devices relative to the baseline. At  $V_{GS} = 5$  V and  $V_{DS} = 12$  V, device D2 achieves  $I_{DSmax}$  of 26.91 mA, nearly  $10.6\times$  greater than the baseline (2.52 mA) and substantially higher than device D1 (17.1 mA). Similarly, the  $g_{mmax}$  is significantly improved with device D2 reaching 6.84 mS, compared to 1.79 mS and 5.46 mS for, respectively, the baseline and device D1. Both optimized devices maintain E-mode operation, with  $V_{th}$  ranging from 0.45 V to 0.49 V. It is worth noting that the  $W_{eff}$  in the proposed devices (and particularly in device D1) is considerably higher than in the baseline, facilitating higher current density. Overall, these results confirm that aggressive structural optimization, when not constrained by expensive simulation costs, can substantially improve  $I_{DS}$  and  $g_m$  while preserving thermal stability and threshold voltage integrity.

As expected in wide devices, both device D1 and device D2 exhibit increased parasitic capacitance compared to the baseline, including gate-to-source capacitance ( $C_{gs}$ ), gate-to-drain capacitance ( $C_{gd}$ ), drain-to-source capacitance ( $C_{ds}$ ), total input capacitance ( $C_{iss} = C_{gs} + C_{gd}$ ), and total output capacitance ( $C_{oss} = C_{gd} + C_{ds}$ ). Notably, device D1 exhibits a significantly lower input capacitance density than the baseline—an important characteristic for power applications that is expected to yield a lower gate drive loss and thus, higher power efficiency at comparable current levels.

According to Table II, based on the  $R_{on}$  results extracted at  $V_{DS} = 0.5$  V, it can be seen that device D2, which has the highest output current, exhibits the lowest value of 37.53  $\Omega$ . Both proposed devices demonstrate a significant improvement compared to the baseline device. Additionally, comparing the proposed devices with the baseline device in terms of the power figure of merit ( $FoM = R_{on} \times (2Q_G + 2Q_{GD})$ ), extracted under small-signal analysis at  $V_{GS} = 5$  V and  $V_{DS} = 6$  V, shows that although the proposed circuits have larger  $C_{iss}$  and  $C_{oss}$  capacitances—and consequently more charge—due to their greater fin height ( $H_{fin}$ ), they still achieve a substantial improvement in FoM as a result of the significant reduction in  $R_{on}$ . In this case, device D2 and device D1, with FoM values of 13.09 p $\Omega$ ·C and 29.5 p $\Omega$ ·C, respectively, achieve improvements of approximately  $10.8\times$  and  $4.79\times$ , respectively, compared to the baseline device, further highlighting the effectiveness of the proposed optimization method.

**Scalable Multi-Fin Configuration.** Multi-fin configurations with 300 identical fins designed using device D1 or device D2 are designed with filling factors (FF) of, respectively, 46% and 44% [13]. A slightly reduced filling factor (compared to 50% in the baseline) is due to the nature of the single-fin configuration of these devices compared to the multi-fin structure in [13]. The current  $I_{DS}$  and parasitics  $R_{on}$ ,  $C_{iss}$ , and  $C_{oss}$  are extracted based on TCAD simulations. A fixed fin spacing ( $S_{fin}$ ) of 100 nm is used for both device designs.

Performance metrics of device D1 as a function of the num-

TABLE II  
COMPARISON OF KEY DC AND AC PARAMETERS FOR SINGLE-FIN  
BASELINE AND OPTIMIZED DEVICES.

Parameter	Baseline [3]	Device D1	Device D2
$W_{eff}$ (nm)	580	1,555	940.1
DC @ $V_{GS}=5$ V, $V_{DS}=12$ V			
$I_{DSmax}$ (mA/mm)	4,351	11,013	28,636
$I_{DSmax}$ (mA)	2.52	17.1	26.91
$g_{mmax}$ (mS/mm)	3,102	3,514	7,287
$g_{mmax}$ (mS)	1.79	5.46	6.84
$R_{on}$ ( $\Omega$ )	704.2	86.8	37.53
$V_{th}$ (V)	0.432	0.491	0.448
AC @ $V_{GS}=0$ V, $V_{DS}=6$ V			
$C_{gs}$ (fF)	0.3672	0.872	0.790
$C_{gs}$ (fF/mm)	633.1	560.7	840.34
$C_{gd}$ (fF)	0.0501	0.165	0.180
$C_{gd}$ (fF/mm)	86.4	106.1	191.47
$C_{ds}$ (fF)	0.0037	0.001	0.0015
$C_{ds}$ (fF/mm)	6.4	0.643	1.60
$C_{iss}$ (fF)	0.4173	1.037	0.97
$C_{iss}$ (fF/mm)	719.5	667.1	1031.81
$C_{oss}$ (fF)	0.0538	0.166	0.1815
$C_{oss}$ (fF/mm)	92.8	106.7	193.06
AC @ $V_{GS}=5$ V, $V_{DS}=6$ V			
$C_{iss}$ (fF)	2.05	4.38	4.05
$C_{oss}$ (fF)	15.04	24.68	25.71
$Q_G$ (fC)	10.25	21.9	20.25
$Q_{GD}$ (fC)	90.24	148.08	154.26
FoM (p $\Omega$ ·C)	141.53	29.5	13.09

TABLE III  
COMPARISON BETWEEN MULTI-DEVICE CONFIGURATIONS BASED ON  
THE PROPOSED DEVICES AND EPC COMMERCIAL PRODUCTS.

Parameter	ML-Optimised Devices				EPC Products		
	Device D1 <sup>1</sup>		Device D2 <sup>1</sup>		2040	2216	2023
	Switch <sup>2</sup>	$50\times^3$	Switch <sup>2</sup>	$50\times^3$			
$C_{iss}$ (pF)	0.18	8.86	0.16	8.15	86	98	2,150
$C_{oss}$ (pF)	0.05	2.44	0.04	1.90	67	66	1,530
$Q_G$ (pC)	5.11	255	5.24	262	745	870	19,000
$Q_{GD}$ (pC)	0.29	14.6	0.23	11.48	140	130	3,200
$Q_{G+GD}$ (pC)	5.4	270	5.47	274	885	1,000	22,200
$R_{on}$ (m $\Omega$ )	490	9.8	940	18.8	24	26	1.45
FoM <sup>4</sup> (p $\Omega$ ·C)	5.29	5.29	10.3	10.3	21.2	26	32.2
$I_{DSmax}$ (A)	3.3	165	1.67	83.5	3.4	3.4	90

<sup>1</sup>w/o extrinsic parasitics <sup>2</sup>300-fin device <sup>3</sup>50 parallel switches <sup>4</sup>lower is better

ber of fins are shown in Fig. 9. As the fin count increases to 300,  $I_{DS}$  rises significantly, exceeding 3.3 A, while  $R_{on}$  drops below 0.5  $\Omega$ . This reflects a substantial improvement in current handling and a reduction in conduction losses. Additionally, the  $W_{eff}$  increases more rapidly than the physical gate width ( $W_g$ ), demonstrating the benefits of vertical multi-channel scaling. These trends confirm that fin scaling efficiently improves the power density of tri-gate GaN structures, optimizing both device size and resistive performance in device D1.

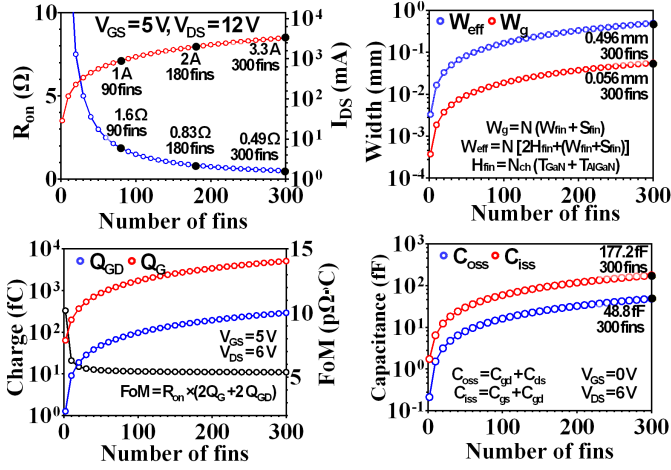


Fig. 9. Design space exploration of device D1 as a function of the number of fins, showing that increasing fin count reduces  $R_{on}$  while increasing  $I_{DS}$ ,  $Q_g$ , and capacitances, leading to a trade-off in switching FoM.

Parasitic capacitance and switching charge behavior for device D1 are shown in Fig. 9. As expected, both  $C_{iss}$  and  $C_{oss}$  increase with the number of fins, but remain within a practical range even at 300 fins. Similarly, the gate charge components  $Q_G$  and  $Q_{GD}$  scale with the larger channel area, though their impact is mitigated by the substantial reduction in  $R_{on}$ . As a result, the power FoM improves, indicating that device D1 achieves high current drive with controlled switching losses—a critical balance for high-performance power-switching applications. As shown in Fig. 10, device D2 also benefits from higher number of fins, yet with lower performance gains compared to device D1. As the fin count increases to 300,  $I_{DS}$  reaches 1.67 A—nearly half of device D1’s current drive, while  $R_{on}$  is reduced to 0.94  $\Omega$ , almost twice as high as the 0.49  $\Omega$  observed in device D1. This indicates that while device D2 exhibits superior single-fin performance, it also exhibits current spreading effects when scaled to multi-fin configurations [9], [12], [13]. As a result, its  $I_{DS}$  and  $R_{on}$  are constrained by the thinner GaN channel, thicker AlGaN barrier, and smaller  $W_{eff}$  and  $W_g$  compared to device D1.

In the 300-fin configuration, device D2 exhibits lower capacitances and switching charges compared to device D1, with  $C_{iss}$  and  $C_{oss}$  reaching, respectively, 163 fF and 38 fF, as shown in Fig. 10. Gate charges  $Q_G$  and  $Q_{GD}$  also remain smaller owing to the device’s reduced channel volume and gate area. Due to its higher  $R_{on}$ , device D2 achieves a worse FoM despite its favorably lower capacitances. This trade-off between the two devices highlights the critical importance of balancing resistive and capacitive parasitic component, and suggests that device D1 is better suited for applications that prioritize power efficiency along with maximum current drive.

**Scalable Multi-Device Configuration.** A system of 50 parallel-connected multi-fin devices is designed and simulated. The results are summarized in Table III alongside several industrial benchmarks. Both proposed devices demonstrate substantial improvements in switching and conduction per-

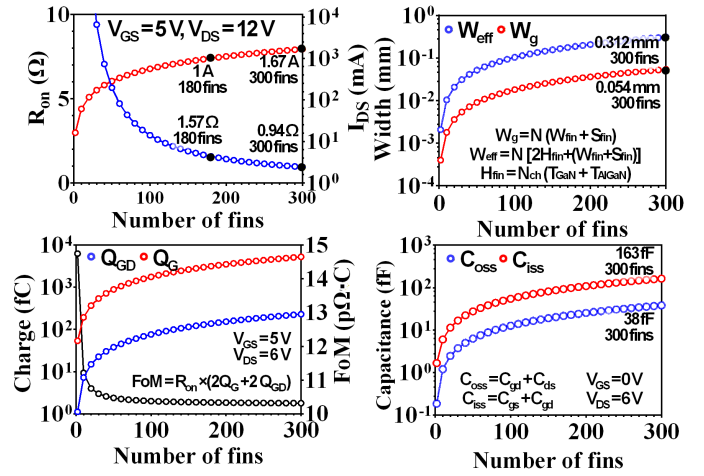


Fig. 10. Design space exploration of device D2 as a function of the number of fins, showing that increasing fin count reduces  $R_{on}$  while increasing  $I_{DS}$ ,  $Q_g$ , and capacitances, leading to a trade-off in switching FoM.

formance over the listed commercial benchmarks. Notably, device D1 achieves  $I_{DSmax}$  of 165 A, nearly double the current capability of the leading commercial device, EPC2023 (90 A), and vastly higher than EPC2040 and EPC2216 (3.4 A each). Furthermore, the device D1-based 300-fin 50-device system exhibits the lowest power FoM, achieving 5.29  $\text{p}\Omega\cdot\text{C}$ , a nearly 6 $\times$  improvement over EPC2023 (32.19  $\text{p}\Omega\cdot\text{C}$ ). This remarkable performance results from both its significantly reduced  $R_{on}$  of 9.8 m $\Omega$  and low gate charge.

Alternatively, device D2 complements these results by exhibiting lower parasitic capacitances, making it more suitable for lower-power voltage regulators where minimizing switching losses is critical. Specifically, device D2 exhibits  $C_{iss} = 8.15$  pF and  $C_{oss} = 1.9$  pF, both lower than, respectively, the 8.86 pF and 2.44 pF for device D1 and over two orders of magnitude smaller than those in EPC2023 ( $C_{iss} = 2,150$  pF,  $C_{oss} = 1,530$  pF). Despite its smaller capacitances, device D2 delivers a high current of 83.5 A, closely matching EPC2023 but at a much lower capacitance and power FoM (10.29  $\text{p}\Omega\cdot\text{C}$  vs. 32.19  $\text{p}\Omega\cdot\text{C}$ ). Importantly, the  $Q_G$  and  $Q_{GD}$  of the proposed devices are significantly lower than those of commercial products. The total charge ( $Q_G + Q_{GD}$ ) of device D1’s is only 270 pC, compared to 22,200 pC for EPC2023—an almost 82 $\times$  reduction, enabling faster switching transitions and lower dynamic losses. Overall, the proposed devices, particularly device D1, achieve high current drive, low on-resistance, and reduced switching losses. These results highlight the potential of optimized multi-fin GaN tri-gate architectures for next-generation power switching.

Finally, the off-state breakdown characteristics of device D1 and device D2 are shown in Fig. 11(a) and (b), extracted at  $I_{DS} = 1$  mA/mm with  $L_{gd} = 0.6$   $\mu\text{m}$  under substrate float conditions. At 25 $^\circ\text{C}$ , device D1 achieves a breakdown voltage of 200 V, while device D2 reaches 94 V. At 150 $^\circ\text{C}$ , these values decrease to 157 V and 64 V, respectively, still maintaining sufficient voltage margins for the targeted applications. These

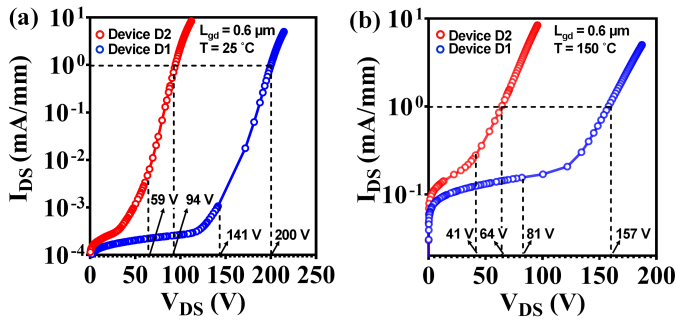


Fig. 11. Off-state breakdown characteristics of (a) device D1 (200 V at 25°C, 157 V at 150°C), and (b) device D2 (94 V at 25°C, 64 V at 150°C).

results highlight device D1's superior thermal stability and voltage robustness for compact embedded power switches.

#### IV. CONCLUSION

Two low-loss, high-current tri-gate FinFET devices with small  $R_{on}$  are proposed in this paper. The devices are optimized using a physics-informed, active learning-based procedure that effectively reduces computational cost and time of otherwise prohibitive TCAD-based simulations. Compared to prior art and commercial off-the-shelf power switches, the resulting devices demonstrate superior performance for power delivery applications, paving the way for further optimization of complex device architectures toward application-specific performance targets.

#### REFERENCES

- [1] S. Krishnakumar, M. Choi, R. R. Khorasani, R. Sharma, M. Swaminathan, S. Kumar, and I. Partin-Vaisband, "Vertical power delivery for high performance computing systems with buck-derived regulators," in *IEEE Electronic Components and Technology Conference (ECTC)*, 2024, pp. 2136–2142, doi:10.1109/ECTC51529.2024.00364.
- [2] S. Krishnakumar and I. Partin-Vaisband, "Vertical power delivery for emerging packaging and integration platforms-power conversion and distribution," in *IEEE International System-on-Chip Conference (SOCC)*, 2023, pp. 1–6, doi:10.1109/SOCC58585.2023.10256973.
- [3] A. Sadeghi and I. Partin-Vaisband, "Analysis and optimization of multi-channel e-mode AlGaIn/GaN Trigate FinFET for vertical power delivery with embedded power converters," in *IEEE Electronic Components and Technology Conference (ECTC)*, 2025, pp. 1282–1289, doi:10.1109/ECTC51687.2025.00220.
- [4] S. Abdelzاهر, M. Gharib, A. R. Trivedi, and I. Partin-Vaisband, "Bandit learning-driven power gating with state retention for high performance computing," in *IEEE 34th Conference on Electrical Performance of Electronic Packaging and Systems (EPEPS)*, 2025, pp. 1–3, doi:10.1109/EPEPS63858.2025.11346621.
- [5] R. Rasheedi and I. Partin-Vaisband, "High aspect ratio spiral inductor with progressive turn widths for embedded power converters," in *IEEE 75th Electronic Components and Technology Conference (ECTC)*, 2025, pp. 2271–2277, doi:10.1109/ECTC51687.2025.00386.
- [6] M. A. Gharib, S. Abdelzاهر, and I. Partin-Vaisband, "An analytical model for high-frequency through silicon vias," in *Proceedings of the Great Lakes Symposium on VLSI (GLSVLSI)*, 2024, pp. 282–286, doi:10.1145/3649476.3658792.
- [7] M. Gharib and I. Partin-Vaisband, "Efficient scalable thermoelectric modeling of high-frequency cylindrical interconnects for heterogeneous package arrays," in *IEEE 75th Electronic Components and Technology Conference (ECTC)*, 2025, pp. 2278–2285, doi:10.1109/ECTC51687.2025.00387.

- [8] R. Rasheedi and I. Partin-Vaisband, "An embedded multi-layer spiral square inductor for integrated power delivery - physical design and analytical models," in *Proceedings of the Great Lakes Symposium on VLSI (GLSVLSI)*, 2024, pp. 370–375, doi:10.1145/3649476.3658746.
- [9] C.-H. Wu, J.-Y. Chen, P.-C. Han, M.-W. Lee, K.-S. Yang, H.-C. Wang, P.-C. Chang, Q. H. Luc, Y.-C. Lin, C.-F. Dee, A. A. Hamzah, and E. Y. Chang, "Normally-off tri-gate AlGaIn/GaN multi-channel FinFET," *IEEE Transactions on Electron Devices*, vol. 66, no. 8, pp. 3441–3446, 2019, doi:10.1109/TED.2019.2922301.
- [10] C.-L. Yu, C.-H. Lin, and Y.-R. Wu, "Analysis and optimization of GaN based multi-channels finfets," *IEEE Transactions on Nanotechnology*, vol. 19, pp. 439–445, 2020, doi:10.1109/TNANO.2020.2998840.
- [11] H.-S. Zhang, X.-H. Ma, M. Zhang, Y. Lu, Q. Zhu, Z.-Y. Zhao, C.-P. Yi, L.-A. Yang, P.-J. Ma, and Y. Hao, "Influence of different fin configurations on small-signal performance and linearity for AlGaIn/GaN Fin-HEMTs," *IEEE Transactions on Electron Devices*, vol. 66, no. 8, pp. 3302–3309, 2019, doi:10.1109/TED.2019.2921445.
- [12] Y. Zhang, F. Udrea, and H. Wang, "Multidimensional device architectures for efficient power electronics," *Nature Electronics*, vol. 5, pp. 723–734, 2022, doi:10.1038/s41928-022-00860-5.
- [13] J. Ma, C. Erine, P. Xiang, K. Cheng, and E. Matioli, "Multi-channel tri-gate normally-on/off AlGaIn/GaN MOSHEMTs on Si substrate with high breakdown voltage and low ON-resistance," *Applied Physics Letters*, vol. 113, no. 24, p. 242102, 2018, doi:10.1063/1.5064407.
- [14] K.-S. Im, R.-H. Kim, K.-W. Kim, D.-S. Kim, C. S. Lee, S. Cristoloveanu, and J.-H. Lee, "Normally off single-nanoribbon Al<sub>2</sub>O<sub>3</sub>/GaIn MIS-FET," *IEEE Electron Device Letters*, vol. 34, no. 1, pp. 27–29, 2013, doi:10.1109/LED.2012.2222861.
- [15] Y. Ma, M. Xiao, Z. Du, H. Wang, and Y. Zhang, "Tri-gate GaIn junction HEMTs: Physics and performance space," *IEEE Transactions on Electron Devices*, vol. 68, no. 10, pp. 4854–4861, 2021, doi:10.1109/TED.2021.3103157.
- [16] S. Abdelzاهر, M. Gharib, and I. Partin-Vaisband, "Hybrid voltage regulators for high performance computing: Analytical models and design methodology," in *IEEE Electronic Components and Technology Conference (ECTC)*, 2025, pp. 2286–2292, doi:10.1109/ECTC51687.2025.00388.
- [17] Y. Xu, S. Cristoloveanu, M. Bawedin, K.-S. Im, and J.-H. Lee, "Performance improvement and sub-60 mV/decade swing in AlGaIn/GaN FinFETs by simultaneous activation of 2DEG and sidewall MOS channels," *IEEE Transactions on Electron Devices*, vol. 65, no. 3, pp. 915–920, 2018, doi:10.1109/TED.2017.2788920.
- [18] L. Nela, J. Ma, C. Erine, P. Xiang, T.-H. Shen, V. Tileli, T. Wang, K. Cheng, and E. Matioli, "Multi-channel nanowire devices for efficient power conversion," *Nature Electronics*, vol. 4, 2021, doi:10.1038/s41928-021-00550-8.
- [19] J. Kwak, S. Deng, J. Lee, S. Datta, and S. Yu, "Backside active power delivery with hybrid dc-dc converter enabled by amorphous oxide semiconductor transistors," *IEEE Transactions on Very Large Scale Integration (VLSI) Systems*, pp. 1–10, 2025, doi:10.1109/TVLSI.2025.3570078.
- [20] M. D. McKay, R. J. Beckman, and W. J. Conover, "A comparison of three methods for selecting values of input variables in the analysis of output from a computer code," *Technometrics*, vol. 21, no. 2, pp. 239–245, 1979. [Online]. Available: <http://www.jstor.org/stable/1268522>
- [21] R. Cipolla, Y. Gal, and A. Kendall, "Multi-task learning using uncertainty to weigh losses for scene geometry and semantics," in *IEEE/CVF Conference on Computer Vision and Pattern Recognition (CVPR)*, 2018, pp. 7482–7491, doi:10.1109/CVPR.2018.00781.
- [22] B. Settles, "Active learning literature survey," University of Wisconsin-Madison, Computer Sciences Technical Report 1648, 2009. [Online]. Available: <http://axon.cs.byu.edu/~martinez/classes/778/Papers/settles.activelearning.pdf>
- [23] B. Lakshminarayanan, A. Pritzel, and C. Blundell, "Simple and scalable predictive uncertainty estimation using deep ensembles," in *Proceedings of the 31st International Conference on Neural Information Processing Systems (NIPS)*, ser. NIPS '17. Red Hook, NY, USA: Curran Associates Inc., 2017, pp. 6405–6416.
- [24] K. Deb, A. Pratap, S. Agarwal, and T. Meyarivan, "A fast and elitist multiobjective genetic algorithm: Nsga-ii," *IEEE Transactions on Evolutionary Computation*, vol. 6, no. 2, pp. 182–197, 2002, doi:10.1109/4235.996017.